DOI: 10.15480/882.9313

Eighth International Symposium on Marine Propulsors
smp'24, Berlin, Germany, March 2024

Experimental study on dynamic forced pitch motions of rigid and flexible hydrofoils in towing tank

Théo Simonet[1], Antoine Ducoin[1], Quentin Rakotomalala[2], Mathias Riou[2], Arnaud Merrien[1], Florent Thiebaut[1], Camille Yvin[3]

[1]Nantes Université, École Centrale Nantes, CNRS, LHEEA, UMR 6598, Nantes, France
[2]Centre d'Expertise des Structures et MAtériaux Navals (CESMAN) Naval Group, Bouguenais, France
[3]SIREHNA, Technocampus Ocean, 5 rue de l'Halbrane, 44340 Bouguenais, France

ABSTRACT

This paper presents a study on the hydrodynamics of rigid and flexible hydrofoils, in dynamic stall regime due to pitching actuation. An original experimental setup was developed to accommodate large scale innovative appendages, in the towing tank at Centrale Nantes, France. The original feature of the setup is its capability to simultaneously induce dynamical pitching motions to the appendages, and use optical fibers with arrays of fiber bragg gratings, for real-time strain monitoring. Forces and moments are measured dynamically with a six degree-of-freedom hydrodynamic balance. In this study, the Reynolds number considered ranged from $Re = 160\,000$ to $1\,000\,000$. The appendages are pitch-actuated with reduced frequencies $k = \pi f c/V$ up to 0.14. Two appendages are considered. The first one is a rigid, thick, rectangular hydrofoil with a low aspect ratio (rudder-like hydrofoil). The second one is a flexible, thin, trapezoidal hydrofoil with a high aspect ratio (simplified propeller blade geometry). The data demonstrated setup capabilities to capture subtle flow phenomena such as as displacement of center of pressure, or delay of stall onset. Finally, the measurements present very good correlation between measured lift coefficients and strains of the flexible hydrofoil.

Keywords

Dynamic stall; Composite hydrofoil; Optical fiber; Towing tank;

1 INTRODUCTION

There is a growing interest for design and optimization of innovative lifting appendages. This stimulation comes from the constant development of devices such as flexible composite propeller blades or wind turbine blades, and new shapes/technologies of ship rudders or hydrofoils. Specifically, 3D dynamic stall phenomena and Fluid-Structure Interaction (FSI), at relatively high Reynolds numbers ($Re \approx 1\,000\,000$), are still not well understood. This lack of knowledge is mainly due to the inherent difficulties to study this phenomena, both experimentally and numerically. On one hand, high-fidelity CFD simulations such as LES (Large Eddy simulation) or DNS (Direct Numerical Simulation) allow precise descriptions of fluid flows in this context (Visbal & Garmann 2018, Shayanpoor et al. 2020), but the computational cost is still too expensive to study large ranges of parameters and/or complex geometries. On the other hand, very few studies concern the interaction between static/dynamic stall and the appendage flexibility, and it is restricted to experiments (Ducoin et al. 2012). Actual facilities are mostly restricted to low Reynolds number, or appendages with low aspect ratios. There is a need for high-quality large scale experimental data to enhance our comprehension of dynamic stall and fluid structure interaction, and to provide test cases to validate numerical methods.

Experimental studies on dynamic stall

The static and dynamic stall phenomenon has been subject to numerous researches in the last 3 decades. The National Renewable Energy Lab. (NREL), published a series of comprehensive reports about static and dynamic stall regimes of various airfoils, with Reynolds number up to $Re = 1\,500\,000$. For examples see (Janiszewska et al. 1996, Ramsay et al. 1995, Hoffmann et al. 1996, Reuss Ramsay et al. 1996). Theses experiments were conducted in a wind tunnel at the Ohio state University. All data are available in open access, on NREL website. There is not yet a consensus in the literature about the influence of the Reynolds number on the dynamic stall phenomenon, see (Choudhry et al. 2014, Gardner et al. 2023) for literature reviews. Some authors found that the Reynolds number play a minor role in dynamic stall (Zhang & Schlüter 2012, Choudhuri & Knight 1996, Robinson & Wissler 1988), while a recent high-fidelity study highlighted the sensitivity of the laminar separation bubble to Reynolds number (Benton & Visbal 2019). Additionally, Choudhry et al. (2014) conjectured that the dynamic stall process is greatly influenced by the state of the boundary layer prior to any unsteadiness. The maximal lift value increasing with the reduced frequency has been widely reported in literature (Choudhry et al. 2014, Jumper et al. 1987, Gardner et al.

2023). This phenomenon is attributed to the detachment of the primary stall vortex, denoted as stall onset, that is delayed to a higher angle of attack when the reduced frequency increases. Mulleners & Raffel (2012) used time resolved particle image velocimetry, with different coherent structure identification methods on a pitching airfoil. The approach enables a precise analysis of the flow field, and led to a better understanding of the stall onset phenomenon ($Re = 900\,000$). The authors proposed a definition based on underlying physical mechanism to differentiate deep and light dynamic stall. That is to say, light dynamic stall occurs when the angle of attack starts decreasing before the dynamic stall onset, while deep stall characteristics are observed otherwise (Mulleners & Raffel 2012). Holst et al. (2019) conduct dynamic 2D experiments at Reynolds numbers up to $Re = 180\,000$. The wind tunnel setup allows the airfoil to rotate with a $180°$ range, enabling the study of all flow regimes encountered by vertical axis wind turbines. Andreu Angulo & Ansell (2019), with an open-return wind tunnel, studied the influence of aspect ratio on dynamic stall of 3D wings. The experimental setup allows wings with aspect ratios up to $AR = 5$ ($Re = 400\,000$). Bøckmann & Steen (2014) and Bøckmann (2015) studied propulsive regimes of a 3D oscillating hydrofoil in a towing tank. The dynamic stall was induced by simple harmonic motions, and combined pitching and heaving motions of the hydrofoil ($AR = 10$, $Re = 200\,000$). In addition, it is now established that dynamic stall process can vary significantly from cycle to cycle due to stochastic variations (Gardner et al. 2023). It has also been observed that variations can be clustered into distinct groups with clear fluctuations (Holst et al. 2019). For a broader overview of dynamic stall phenomenology, the reader can refer to the recent literature review of Gardner et al. (2023). The review cover dynamic stall experiments, from flight tests to pitching airfoils. It appears that very few experimental data is available on the dynamic stall of marine profiles at relatively large scale.

Experimental studies on FSI of lifting device

The study of fluid structure interaction for marine application has been the subject of growing interest with the development of composite profiles, which aim to passively control deformations to enhance performances. It often combines simulations and experiments. Akcabay et al. (2014) compares experiments in cavitation tunnel with RANS simulations (two degrees of freedom system), to study the influence of cavity-induced vibrations on a static NACA66 hydrofoil, below stall incidence (2D, $Re = 750\,000$). The cavitation dynamics and its influence on hydrofoil's deformation were highlighted. Zarruk et al. (2014) studied hydroelastic performance of composite hydrofoils in static condition beyond stall in a water tunnel ($AR = 3.33$, $Re = 1\,000\,000$). Young et al. (2018) conduct a study about bend-twist coupling effects on the steady-state hydroelastic response of composite hydrofoils, below and above stall incidence ($AR = 3.33$, $Re = 1\,200\,000$). In the same water tunnel facility, Herath et al. (2021) characterised the hydrodynamic response of an optimised passive shape-adaptable composite hydrofoil. FSI simulations were performed to comfort the findings. Numerical results were observed to closely match the experimental hydrodynamic results and structural deformations. The study highlighted the better performances of the optimised hydrofoil, compared to others ($AR = 3.33$, Re up to $1\,000\,000$). Pernod et al. (2019) investigate the hydroelastic response of a composite hydrofoil below and above stall incidence. Hydrofoil strains were measured by a fully-distributed-optical fiber sensor within the composite plies. Good correlation was achieved with a tightly-coupled high-fidelity fluid-structure interaction numerical model ($AR = 2.13$, $Re = 540\,000$). Bi & Cai (2012) conducted experiments in a water tank to investigate the influence of spanwise flexibility of hydrofoils, in the context of bio-mimetic propulsion. Hydrofoils were subjected to a rolling motion, in order to mimic fish pectoral fins ($AR = 2$, $Re = 20\,000$). In the same context of bio-mimetic propulsion, Heathcote et al. (2008) and also Cleaver et al. (2016) studied the influence of spanwise flexibility of heaving hydrofoils ($AR = 1.5{-}3$, $Re = 10\,000 - 30\,000$). Heathcote et al. (2008) used a high speed video camera and a motion-tracking software to measure the hydrofoils deformation. This experiment became a notable benchmark for fluid-structure code validation, either for full FSI methods (Gordnier et al. 2013, Cho et al. 2019), or methods with imposed deformation of hydrofoils (Faure et al. 2022, Simonet et al. 2020). The correspondence between experimental and numerical results is mainly well established. The exception is for the most flexible hydrofoil, for which the trust coefficient exhibits high frequency oscillations, still not explained today. Recently, Young et al. (2023) conduct experiments in the large depressurized wave basin at MARIN (Netherlands), to study hydrodynamics of a flexible surface-piercing hydrofoil in waves. The experimental setup enabled the investigation of the effect of waves and ventilation on structural dynamics.

Fiber bragg grating for measurement of deformation

In order to get precise information about structural deformation, the use of Fiber Bragg Gratings (FBG) has shown satisfactory results for strain measurements (Ducoin et al. 2023, Seaver et al. 2006, Phillips et al. 2017). FBG has also been used to detect and characterize damage in composites (Cook et al. 2017, Yeager et al. 2017). Optical fibers with arrays of FBG are lightweight and small in size. It can be embedded in the composite appendage during the manufacturing process (Seaver et al. 2006, Ducoin et al. 2023), or glued to the surface after manufacturing (Phillips et al. 2017). (Ducoin et al. 2023) conducted steady and unsteady measurements on a composite propeller blade. Optical fibers with arrays of FBG were embedded in each of the pressure and suction sides of the blade. The authors got good agreement between experimental and numerical natural frequencies and were able to measure flow events, and structural vibrations within the strain signals.

The aim of this paper is to present a new experimental setup in the towing tank of Centrale Nantes, France. The setup has been designed to study hydrodynamics of large scale innovative appendages (span$\times$chord $\approx 1 \times 0.5\,\mathrm{m}$, $Re \approx 1\,000\,000$). The appendages can be dynamically pitched

with an amplitude $\alpha_{max} = \pm 45°$. The system is equipped to receive and process signals of optical fibers from appendages, for strain measurements. A study has been conducted on the influence of the Reynolds number, and the reduced frequency, on hydrodynamics of two pitching appendages, in dynamic stall regimes. The first appendage is a rigid rudder-like hydrofoil. The second one is a composite trapezoidal hydrofoil (simplified propeller blade geometry), equipped with optical fibers with arrays of FBG.

2 MATERIALS AND METHODS

2.1 Experimental Setup

The towing tank at Centrale Nantes is $140\,\mathrm{m}$ long, by $5\,\mathrm{m}$ wide, and with a constant depth of $3\,\mathrm{m}$. The tank carriage has a maximum velocity of $8\,\mathrm{m/s}$. The original experimental setup is installed on a dedicated and effectively rigid metal frame, fixed to the carriage (see Fig. 1). The rotating motion is generated along the horizontal direction with a AKM2G-41XLANCN2-0V servo motor from Kollmorgen, which is coupled with a reduction gearbox. The motion is redirected by an angle drive to get the desired pitching motion in the vertical direction (see Fig. 1). A FX2.6 6-components hydrodynamic balance, from Sixaxes, transmits the motion to a clamping mechanism designed to accommodate various types of appendages (see Fig. 2). A flat-bottomed hull is fixed to the frame to limit free surface effects (see Fig. 3). The hull is made of wood and is $5\,\mathrm{m}$ long, $0.5\,\mathrm{m}$ wide, and $0.6\,\mathrm{m}$ high. A reaming has been realised in the bottom of the hull to allow the clamping mechanism to pass through. The full experimental setup is represented in Figure 4.

The balance measures forces (F_x, F_y, F_z), and moments (M_x, M_y, M_z), at the appendage root, where the x-axis is in the chordwise direction, the z-axis is in the spanwise direction, i.e. the vertical direction, and the y-axis completes the orthonormal trihedron. The loading is then projected into the carriage coordinate system to compute the hydrodynamic coefficients. The sampling rate of the hydrodynamic balance is $1000\,\mathrm{Hz}$. The maximum forces and moments and the corresponding maximal uncertainties given by the vendor, are listed in Table 1.

2.2 Rigid and flexible appendages

In the present work, hydrodynamics of two appendages are investigated. The first appendage has a geometry similar to ship rudders. It is a thick, rigid, rectangular hydrofoil made of aluminium. The cross section is the NACA0020, and the aspect ration is $AR = 2$ (see Fig. 5). This rudder-like hydrofoil will be referred to as the rigid hydrofoil. The second appendage has been designed to be representative of a simplified flexible propeller blade. It is a trapezoidal hydrofoil with a straight trailing edge. The cross section is the NACA0006, and the taper ratio and aspect ratio are respectively $TR = 0.3$ and $AR = 6.15$ (see Fig. 6). This simplified propeller blade will be referred as the flexible hydrofoil. The rigid and flexible hydrofoils were initially chosen for unrelated studies, their respective results will be presented but are not intended to be compared.

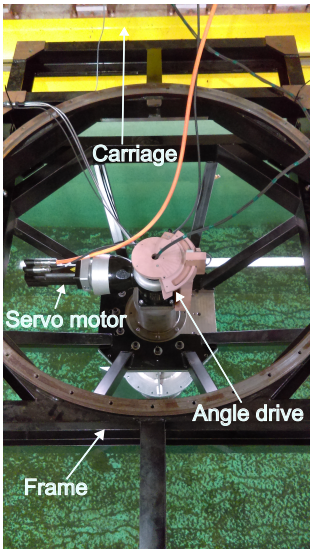

Figure 1: Top view of the experimental setup.

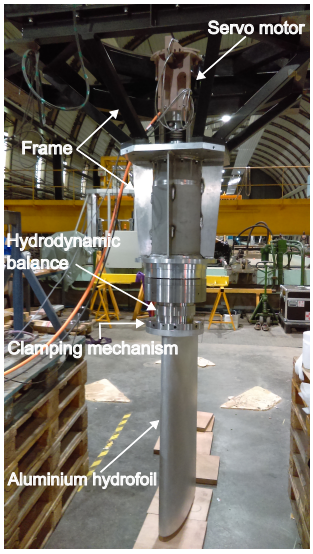

Figure 2: Out of water experimental setup, without hull.

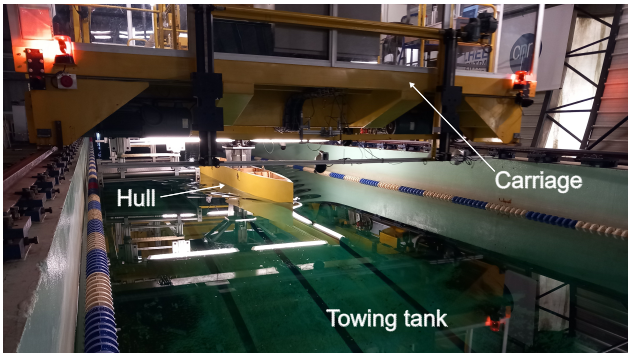

Figure 3: Towing tank with experimental setup.

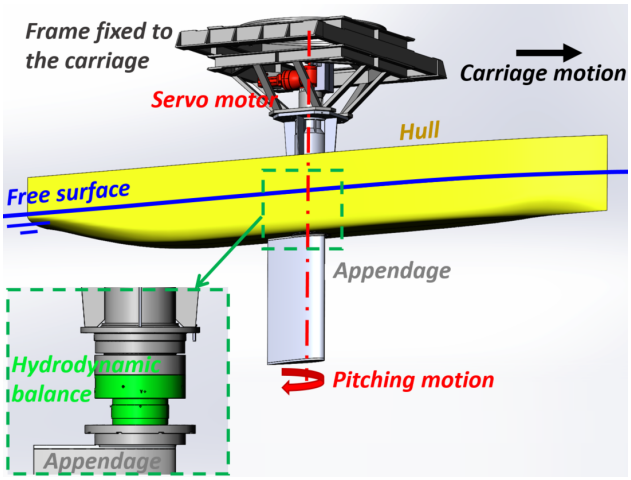

Figure 4: Full experimental setup representation.

Table 1: Balance specifications.

	F_x	F_y	F_z	
Max. loading	400	2000	2000	N
Uncertainty	$\pm$ 5.61	$\pm$ 6.32	$\pm$ 4.11	N
	M_x	M_y	M_z	
Max. loading	1200	240	100	$N.m$
Uncertainty	$\pm$ 2.47	$\pm$ 0.62	$\pm$ 0.61	$N.m$

The flexible hydrofoil was manufactured using prepreg Carbon fiber-reinforced epoxy. Around twenty layers of prepreg were used, alternating between unidirectional and woven layers. The orders of magnitude of the main homogenized material properties are shown in Table 2.

Table 2: Homogenized material properties of the composite flexible hydrofoil (order of magnitude).

Elastic modulus	Shear modulus	Poison's ratio
$E_1 \approx 60\,GPa$	$G_{12} \approx 20\,GPa$	$\nu_{12} \approx 0.7$
$E_2 \approx 20\,GPa$		

Figure 5: Aluminium rigid hydrofoil.

Figure 6: Composite flexible hydrofoil.

In order to assess hydrofoil deformation, two optical fibers with arrays of fiber bragg gratings have been glued on the hydrofoil's surface, for strain measurement (see Fig. 6). A total of 16 fiber optic sensors are distributed over the hydrofoil surface. The data from one sensor are presented in this paper. Figure 7 shows the position of the concerned sensor by a green dot on the hydrofoil's surface. The strain measured corresponds to spanwise flexion. The systematic uncertainty of the strain measurements has been quantified by comparison with strain gauges, on another setup. The measurements showed a strain deviation lower than 3%. The deformations measured with the optical fibers are obtained with a FS22DI interrogator from HBM. The interrogator has a sampling frequency of $1000\,\mathrm{Hz}$, with a wavelength measurement ranging from $1500\,\mathrm{nm}$ to $1600\,\mathrm{nm}$.

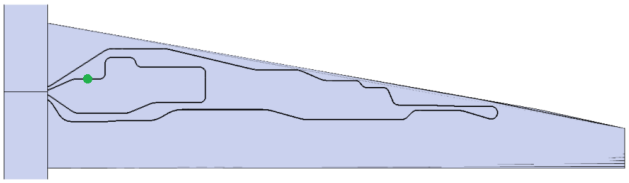

Figure 7: Flexible hydrofoil surface with arrays of fiber bragg gratings. The green dot shows the position of the sensor used in this paper.

2.3 Towing Tank Testing Procedure

For this study, tests were performed at velocities $V = 0.5 - 3\,\mathrm{m/s}$, leading to Reynolds numbers, based on the mean chord length, ranging from $Re = 160\,000$ to $Re = 1\,000\,000$. Considering that there is no incoming turbulence intensity, there could be likely some transitional regimes, in particular for the lower Reynolds number and low angles of attacks.

Static, quasi-static, and dynamic tests have been carried out. For dynamic tests, the hydrofoils were harmonically pitched with a zero average angle of attack: $\alpha = \alpha_{max}\sin(2\pi ft)$, where α is the angle of attack, α_{max} is the pitching amplitude, and f is the oscillating frequency. Reduced frequencies up to $k = \pi f\bar{c}/V = 0.14$ were considered, where $\bar{c}$ is the mean chord length. The pitching amplitudes were chosen to encompass static stall angles, i.e. $\alpha_{max} = 25°$, and $\alpha_{max} = 15°$, for NACA0020 (rigid hydrofoil), and NACA0006 (flexible hydrofoil) respectively. Quasi-static tests correspond to dynamic tests with the lowest reduced frequency permitted by the tank length, i.e. $k = 0.008$. The tank was allowed to settle for about 10 minutes between each test to avoid large-scale vortices induced by the previous run. Each test has been repeated between 1 and 4 times depending on the test type.

The uncertainty analysis performed in this work follows the methods outlined in ASME PTC 19.1- 2005 (Dieck 2014). In the dedicated sections, the mean results come with a total uncertainty, denoted U_{tot}. This total uncertainty results from random and systematic errors. Random errors come from inherent fluctuations of a measured quantity D, and electrical noise in the system. The corresponding uncertainty is quantified as the standard deviation $s_{\bar{D}}$ of the averaged given quantity, through test repetition. Systematic uncertainties, denoted U_{CD}, depends on instrument calibration and sensitivity, as specified by the sensor vendor (see Tab. 1). As the quantities of interest result from combinations of sensor channels, the systematic uncertainties are combined accordingly. As an example, the uncertainty on the lift coefficient, U_{C_L}, is computed as:

$$U_{C_L} = \frac{U_{F_x}|\sin(\alpha)| + U_{F_y}\cos(\alpha)}{\frac{1}{2}\rho V^2 S} \tag{1}$$

Where U_{F_x} and U_{F_y} are the systematic uncertainties of the forces F_x and F_y, measured by the hydrodynamic balance. Finally, the data presented in the dedicated sections come with the 95% confidence intervals computed as $0.95 \times U_{tot}$, where the total uncertainty is given by $U_{tot} = \sqrt{s_{\bar{D}}^2 + U_{CD}^2}$. The confidence intervals are repre-

sented by error bars for static results, and by color strips for quasi-static and dynamic results.

2.4 Noise and filtering

Spectral analysis has been conducted in order to depict the dynamic excitation originating from the experimental setup itself. Figure 8 shows the lift spectra obtained from static tests, with the rigid foil pitched at a constant angle of $25°$. Spectra are normalised and shifted for readability. Two vibration components have been identified. The first one corresponds to the rail plates presence ($V/f = 0.72\,\mathrm{m}$), and have already been observed in previous studies using the towing tank at Central Nantes (Ducoin et al. 2023, Kerdraon et al. 2021). This frequency is proportional to the carriage velocity, as shown in Figure 8. The second vibration component has a constant frequency of $5.1\,\mathrm{Hz}$, and is attributed to the natural frequency of the metal frame.

Part of the lower frequencies observed can be associated to carriage superstructure vibrations, or with a difference in the planarity along the towing tank rail. However, these vibration components are too close to the frequency range of interest to be filtered out. In order to filter noise while preserving main physical information, data from dynamic and quasi-static runs have been smoothed using a linear regression over a moving time window. The window size used ranges from $0.2\,\mathrm{s}$ to $1\,\mathrm{s}$ according to the carriage speed.

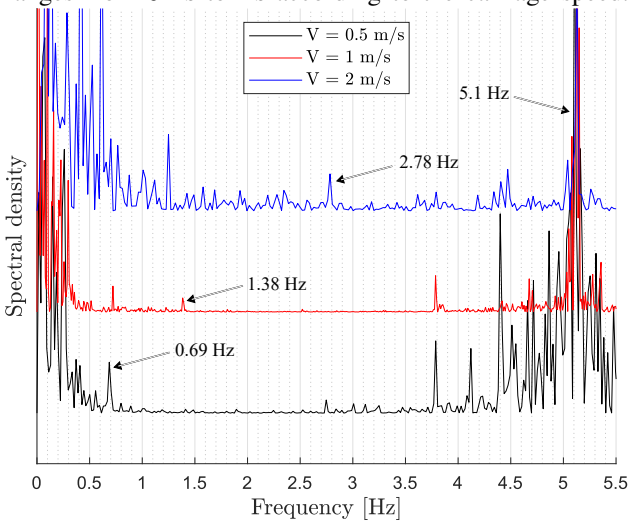

Figure 8: Comparison of lift spectra obtained from static runs, with the rigid foil pitched at a constant angle of $25°$.

2.5 Validation

The reliability of the experimental setup is assessed through comparison with literature data. Static and dynamic lift coefficients from subsonic wind tunnel experiments are considered. The static data come from Paula (2016), and Abrantes et al. (2017). The authors used respectively a pseudo-2D NACA0020 airfoil, and a similar rectangular foil with aspect ration $AR = 2$, operating at Reynolds numbers $Re = 200\,000$ and $290\,000$. The dynamic results are taken from Holst et al. (2019). The authors used a pseudo-2D NACA0021 airfoil pitched from its quarter-chord with a reduced frequency $k = 0.05$, and a Reynolds number $Re = 140\,000$. These data are compared with present results obtained with the rigid hydrofoil operating at $Re = 250\,000$, and $k = 0.05$ for dynamic case.

The quasi-static and static results are shown on Figure 9. The dashed-line from the quasi-static result indicates the decreasing phase of the angle of attack. The present values lie slightly lower than the 3D results from Abrantes et al. (2017). This may come from the different blockage effects in both experiments. The 3D effect appears however well predicted compared to 2D curves that lie closer to the theoretical 2D thin airfoil law (dash-dotted line). The quasi static and static lift coefficients are very close from each other, which demonstrates the measurements accuracy.

The dynamic results are shown on Figure 10. The data from Holst et al. (2019) correspond to airfoil harmonically pitched in light dynamic stall regime (from $0°$ to $20°$, green curve), and deep dynamic stall regime (from $10°$ to $30°$, red curve). The present data correspond to a pitched cycle from $-25°$ to $25°$. The curve hysteresis coincides with the light dynamic stall regime. Additionally, the correspondence of the maximal lift coefficient, reached at around $\alpha = 25°$, with the deep dynamic stall regime, is satisfactory.

The results of Fig. 9 and 10, come with considerable uncertainties. This is due to the low speed required with the carriage, to operate at Reynolds number $Re = 250\,000$, with the rigid hydrofoil. The low hydrodynamic loadings obtained are associated with maximal uncertainties, based on the full measuring range (see Tab. 1). However, the variability through test repetitions is very satisfactory, leading to significantly smaller uncertainties for higher carriage velocities. As an example, hydrodynamic coefficients with uncertainties for a close configuration are shown on the following Results section.

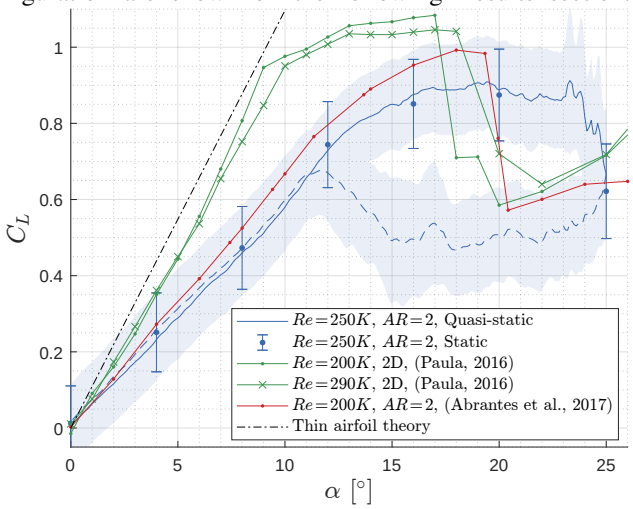

Figure 9: Comparison of static lift coefficient from present experiments and literature data. Dashed-line indicates the decreasing phase of the angle of attack.

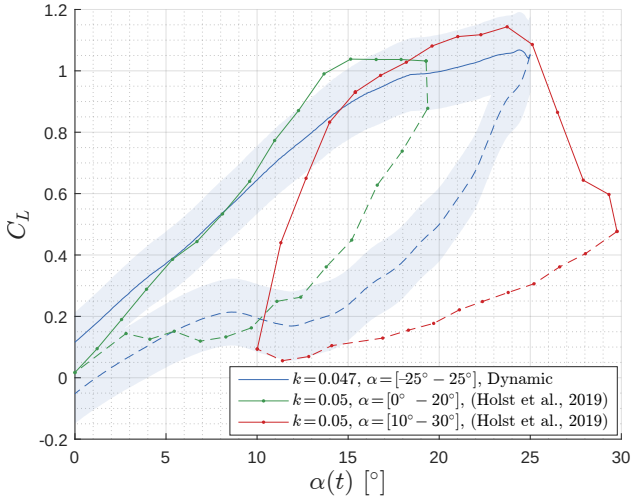

Figure 10: Comparison of dynamic lift coefficient from present experiments and literature data. Dashed-line indicates the decreasing phase of the angle of attack.

3 RESULTS AND DISCUSSION

3.1 Rigid Aluminium Hydrofoil Results

The dynamic stall regime of the hydrofoils is studied by means of the influence of Reynolds number and reduced frequency. The rigid hydrofoil is harmonically pitched around its quarter chord with a pitching amplitude $\alpha_{max} = 25°$. The Reynolds numbers considered are $Re = \{250\,000, 500\,000, 1\,000\,000\}$. The reduced frequencies considered are $k = \{0.02, 0.05, 0.14\}$.

Figure 11 shows the dynamic lift coefficient C_L, and the pitching moment coefficient C_{mz}, obtained at the low reduced frequency $k = 0.02$, and for the various Reynolds numbers considered. The uncertainties for $Re = 500\,000$ and $1\,000\,000$ are show as an indication. For readability purposes, uncertainties for $Re = 250\,000$ (see Fig. 9) are not shown, as well as for all other results. All lift coefficients are very close from each other and show a linear behavior between $-10° \leq \alpha \leq 10°$, which is the consequence of mostly attached boundary layer flow along the chord. Starting from $\alpha \approx 10-11°$, the slope of lift coefficient at $Re = 250\,000$ slightly increases, followed by a clear decrease at about $\alpha \approx 13°$, highlighting a classical trailing edge flow detachment up to the maximum angle of attack. The development of trailing edge detachment is supported by the sudden break of C_{mz} after $\pm 10°$ (see Fig. 11b). It is clearly identified as a displacement of center of pressure toward the trailing edge due to development of detached boundary layer. This behavior is reduced at $Re = 500\,000$ and $Re = 1\,000\,000$, because of Reynolds effects. These two higher Reynolds number show a critical angle of attack of about $\alpha \approx 21°$, which is less visible at $Re = 250\,000$, but stays around the same angle of attack.

For $Re = 250\,000$, C_L exhibits a sudden drop at the maximal angle of attack, probably due to leading edge vortex shedding, observed for both increasing and decreasing angles of attacks. Large Hysteresis is present as flow reattachment process around $\alpha = 10°$. As expected, the hysteresis effect is reduced as the Reynolds number increase.

The influence of Reynolds number is significant from $Re = 250\,000$ to $Re = 500\,000$, whereas it is reduced between $Re = 500\,000$ and $Re = 1\,000\,000$. This observation support the conjecture of Choudhry et al. (2014), that says that the dynamic stall process is greatly influenced by the state of the boundary layer prior to any unsteadiness. As there is no or low incoming turbulence intensity, there could be some highly transitional regimes in particular at $Re = 250\,000$, as portrayed by the non-linearity on C_L at $\alpha \approx 10°$, in Fig. 11a.

Figure 12 shows C_L and C_{mz}, for $Re = 250\,000$, and various reduced frequencies. $k = 0.02$ is considered as a low dynamic case, $k = 0.05$ has moderates dynamic effects and $k = 0.14$ is considered as a fast dynamic case. As k increases, the profile acceleration becomes dominant on the lift and moment coefficients. Hence, the viscous effects are reduced, and consequently the hysteresis progressively disappears. It is highlighted by the sharp decrease of C_{mz} after $\alpha \approx 18°$ for $k = 0.02$, which disappear at $k = 0.14$. The maximal values of C_{mz} are reached at $\alpha = 0°$, where the pitching velocity is maximal. In contrast, for lower k, maximal values of C_{mz} are reached at $\alpha = \pm\alpha_{max}$.

The maximal values of C_L increasing with k is consistent with the literature, and is attributed to the delay of stall onset, (Choudhry et al. 2014, Jumper et al. 1987, Gardner et al. 2023). In addition, the flow reattachment process tends to disappear with increasing k, leading to a practically convex C_L curves for $k = 0.14$ (see Fig. 12a). This characteristic has been extensively designated as light dynamic stall, (McCroskey et al. 1981, Choudhry et al. 2014). The more precise definition of light and deep dynamic stall proposed by Mulleners & Raffel (2012) is based on the stall onset. In their work, Mulleners & Raffel (2012) used proper orthogonal decomposition to determine stall onset. In the present work, stall onset can not be precisely identified, but it appears with the appearance of the hydrodynamic loading, that the transition between deep dynamic stall and light dynamic stall occurs between $k = 0.05$ and $k = 0.14$.

Despite stochastic variations from cycle to cycle and from test repetition, data tend to cluster to a single averaged behavior, which contrasts with the observations of Holst et al. (2019). The reason may come from the finite number of oscillations permitted by the tank length, or also by the significant 3D effects, promoting a particular group of fluctuations.

3.2 Flexible composite Hydrofoil Results

The flexible hydrofoil is harmonically pitched around the mid-chord of the root section, with a pitching amplitude $\alpha_{max} = 15°$. Due to a minor measurement error in the zero lift angle of attack, an offset of $0.25°$ is present, and the angle of attack was oscillating from $-15.25°$ to $14.75°$. The Reynolds numbers considered are $Re = \{160\,000, 330\,000, 500\,000\}$. The reduced frequencies considered are $k = \{0.01, 0.03, 0.1\}$.

Figure 13 shows the dynamic lift coefficient, and the strain measured on the flexible hydrofoil pitched at reduced fre-

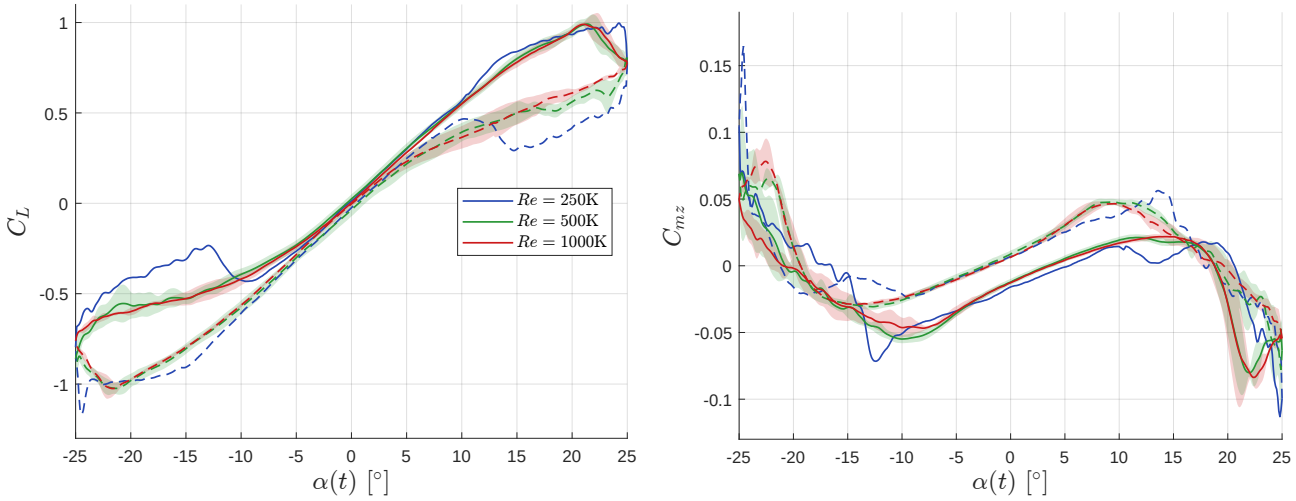

(a) Lift coefficient. **(b) Pitching moment coefficient.**

Figure 11: Dynamic hydrodynamic coefficients ($k = 0.02$, various Re, rigid hydrofoil). With uncertainties color strips for $Re = 500\,000$ and $1\,000\,000$.

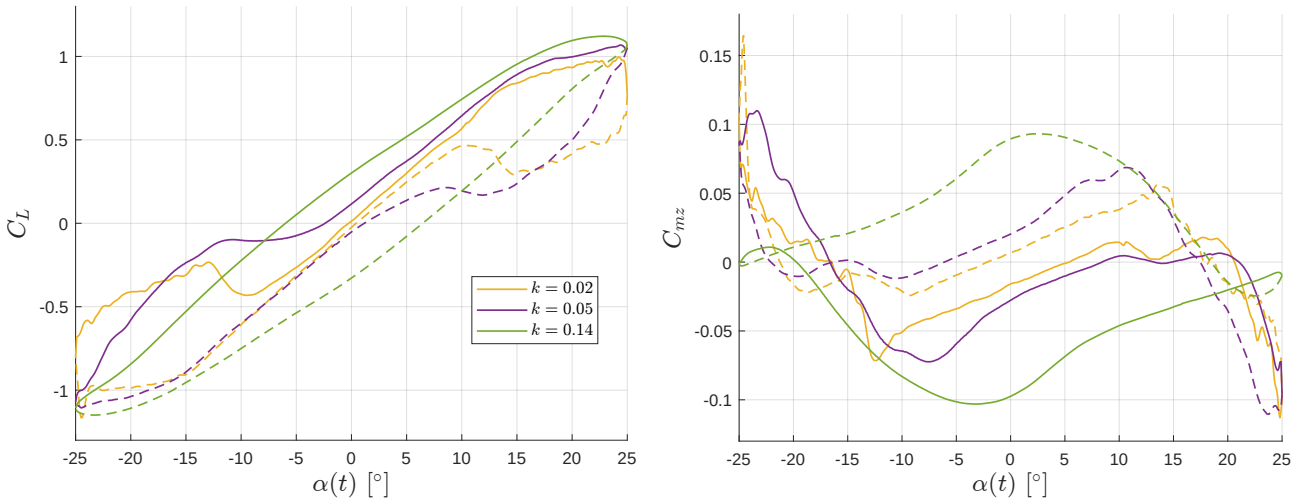

(a) Lift coefficient. **(b) Pitching moment coefficient.**

Figure 12: Dynamic hydrodynamic coefficients (various k, $Re = 250\,000$, rigid hydrofoil).

quency $k = 0.03$, and for the various Reynolds numbers considered. The strains have been normalized by the corresponding carriage velocity squared. It is observed on both the lift coefficient and the strain that the stall is slightly delayed as Reynolds number increases. It is reached at about $\alpha = 12.5°$, 13° and 13.5° for $Re = 160\,000$, $Re = 330\,000$ and $Re = 500\,000$, respectively. After stall, hysteresis effects are observed, which are also reduced as Reynolds number increases. It has to be noted that there is a very high correlation between the lift and strain curves.

Figure 14 shows C_L and strains, for $Re = 330\,000$, and the various reduced frequencies considered. As observed for the rigid, NACA0020 hydrofoil, the reduced frequency plays a major role in the stall behavior. Stall is observed at respectively $\alpha = 11°$, 12.5° and 14.8° for $k = 0.01$, 0.03 and 0.1. As discussed for the rigid hydrofoil, the maximal values of C_L increasing with k is attributed to the delay of stall onset, (Choudhry et al. 2014, Jumper et al. 1987, Gardner et al. 2023). The lower dynamic case ($k = 0.01$) shows that minor hysteresis effect is present on the flexible hydrofoil. After stall, the $k = 0.03$ case shows higher hysteresis due to the combination of boundary layer massive detachment and the profile acceleration. The viscous effects completely vanish for $k = 0.1$ and the shape of lift coefficient and strain is purely due to the dynamic motion.

Again, good correlation between C_L and strains must be highlighted. The deformation of the hydrofoil mainly consists of the first bending mode induced by lift force. Thus, the close proximity of measured stains and C_L reveals the good accuracy of the measurements. Both deformations dominated by viscous effects, and dynamic effects, are well captured (see Fig. 14b).

Considering both appendages, the dynamic stall phenomenon occurring on rigid and flexible hydrofoils, appears to be significantly different. While a sudden stall

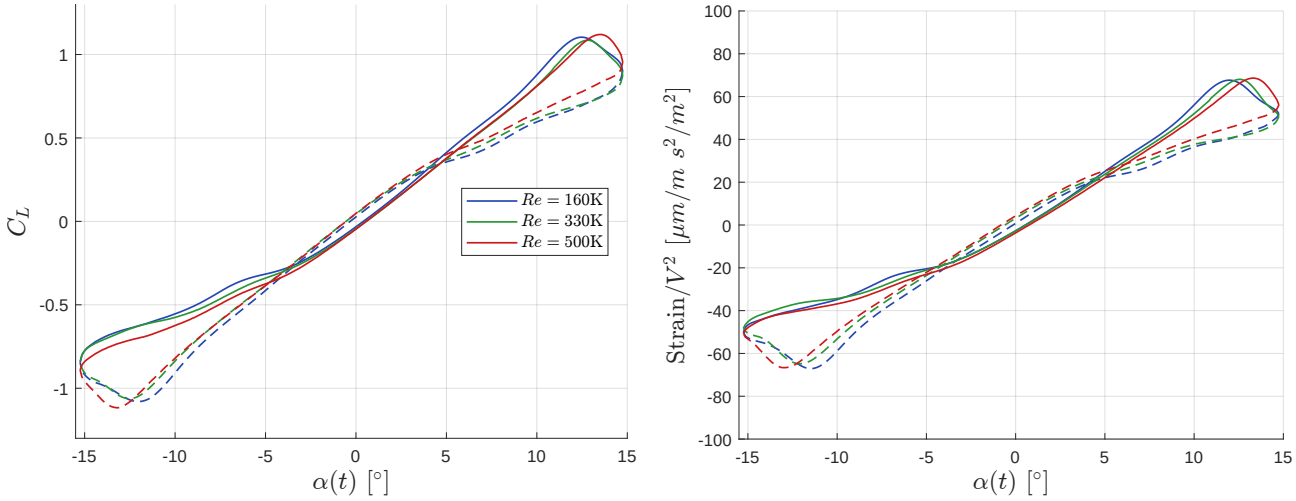

(a) Lift coefficient. **(b) Strain.**

Figure 13: Dynamic lift coefficient and strains ($k = 0.03$, various Re, flexible hydrofoil).

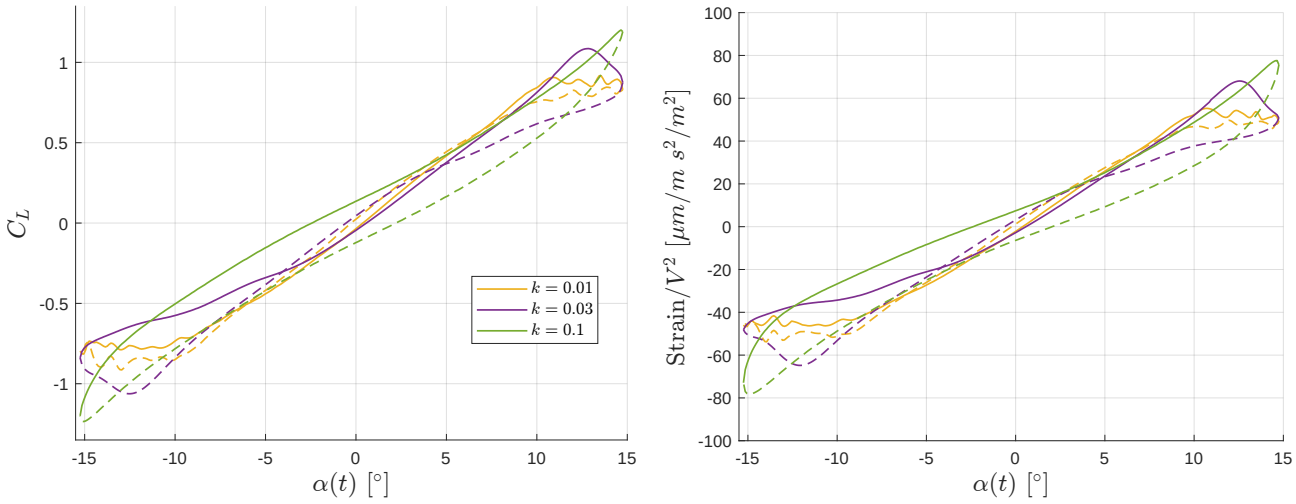

(a) Lift coefficient. **(b) Pitching moment coefficient.**

Figure 14: Dynamic lift coefficient and strains (various k, $Re = 330\,000$, flexible hydrofoil).

occurs for the flexible hydrofoil (see Fig. 13a, 14a), the lift slope of the rigid hydrofoil decreases slowly before stalling (see Fig. 11a, 12a). This illustrates the concept of *leading edge stall*, contrasted with *trailing edge stall*, as discussed by Gardner et al. (2023) and Gupta & Ansell (2020). Thick profiles, as the NACA0020 (rigid hydrofoil), display usually a separation region that grows from the trailing edge towards the leading edge. Depending on the motion, the stall can occur from the convection of a vortical structure resulting from the merging of the trailing edge and the leading edge vortices, (Gupta & Ansell 2020). On the other hand, for thin profiles, as the NACA0006 (flexible hydrofoil), the separation region grows usually from the leading edge, while the flow in the trailing edge region remains attached. The flow then separates rapidly, resulting in a more abrupt stall (see Fig. 13a, 14a). As for the faster dynamic cases, the rigid and flexible hydrofoils does not show the same slopes of the lift coefficient. It can be attributed to the different axis of rotation. The rectangular rigid hydrofoil pitches at the quarter-chord from the leading edge, whereas the flexible hydrofoil pitch at the mid chord from the root section. Considering the flexible hydrofoil's shape, the mean axis of rotation is actually closer to the trailing edge, which modifies substantially the pressure distribution due to the hydrofoil's acceleration as compared to the rigid hydrofoil.

4 CONCLUSIONS

In this paper, an innovative setup that operates in the towing tank at Centrale Nantes, was presented. The setup has been developed to measure the hydrodynamics of relatively large scale innovative appendages (span×chord $\approx 1 \times 0.5\,\mathrm{m}$, $Re \approx 1\,000\,000$). The original feature of the setup is its capability to simultaneously induce dynamical pitching motions to the appendages, and receive and process signals of optical fibers, for strain measurements. Experimental setup capabilities were demonstrated with a study on the influence of the Reynolds number, and the reduced frequency,

on hydrodynamic coefficients and strains of two pitching appendages, in dynamic stall regimes. The first appendage is a rigid rudder-like hydrofoil, while the second one has the geometry of a simplified propeller blade. The latter is made of prepreg Carbon fiber-reinforced epoxy, and it is equipped with optical fibers with arrays of fiber bragg gratings, for strain measurements.

It has been observed, for both rigid and flexible hydrofoils, that increasing reduced frequency, the dynamic effect become dominant as compared to viscous effect. For high reduced frequencies, no hysteresis are observable on lift and moment coefficients. Reynolds effects have been observed mostly on the rigid NACA0020 hydrofoil, whereas they are reduced for the flexible hydrofoil, which has a thinner section. The data demonstrated setup capabilities to capture subtle flow phenomena such as displacement of center of pressure, or delay of stall onset. Finally, as the lift coefficient and the strains are assessed with independent measurement systems, their close proximity demonstrates the great accuracy of the experimental setup.

In our imminent investigations, spectral analysis of signals will be addressed, along with fluid structure interaction phenomena. In the near future, more sophisticated appendages will be tested, and instrumentation for flow measurement will be added to the setup.

ACKNOWLEDGEMENTS

This work was founded by the Carnot MERS institute (APHINOV project), and the Joint Laboratory in Maritime Technology (JLMT), which is a collaboration agreement between Centrale Nantes and Naval Group. The authors would like to thanks all the technicians and engineers from these institutions who contributed to the design and mounting of the experimental setup and the help during measurements.

REFERENCES

Abrantes, T. T. D., Rios Cruz, A. A., de Paula, A. A., Kleine, V. G. & Büttner, F. (2017), The wing three-dimensional effects on wavy leading edge performance, *in* '35th AIAA applied aerodynamics conference', p. 4467.

Akcabay, D. T., Chae, E. J., Young, Y. L., Ducoin, A. & Astolfi, J. A. (2014), 'Cavity induced vibration of flexible hydrofoils', *Journal of Fluids and Structures* **49**, 463–484.

Andreu Angulo, I. & Ansell, P. J. (2019), 'Influence of aspect ratio on dynamic stall of a finite wing', *AIAA journal* **57**(7), 2722–2733.

Benton, S. & Visbal, M. (2019), 'The onset of dynamic stall at a high, transitional reynolds number', *Journal of Fluid Mechanics* **861**, 860–885.

Bi, S. & Cai, Y. (2012), 'Effect of spanwise flexibility on propulsion performance of a flapping hydrofoil at low reynolds number', *Chinese Journal of Mechanical Engineering* **25**(1), 12–19.

Bøckmann, E. (2015), Wave Propulsion of Ships, PhD thesis, NTNU.
URL: *https://ntnuopen.ntnu.no/ntnu-xmlui/handle/11250/284142*

Bøckmann, E. & Steen, S. (2014), 'Experiments with actively pitch-controlled and spring-loaded oscillating foils', *Applied Ocean Research* **48**, 227–235.

Cho, H., Lee, N., Shin, S.-J. & Lee, S. (2019), 'Extensive 3d analysis for fluid–structure interaction of spanwise flexible plunging wing 3d fsi analysis for spanwise flexible plunging wing', *The Aeronautical Journal* **123**(1262), 484–506.

Choudhry, A., Leknys, R., Arjomandi, M. & Kelso, R. (2014), 'An insight into the dynamic stall lift characteristics', *Experimental Thermal and Fluid Science* **58**, 188–208.

Choudhuri, P. G. & Knight, D. (1996), 'Effects of compressibility, pitch rate, and reynolds number on unsteady incipient leading-edge boundary layer separation over a pitching airfoil', *Journal of Fluid Mechanics* **308**, 195–217.

Cleaver, D., Calderon, D., Wang, Z. & Gursul, I. (2016), 'Lift enhancement through flexibility of plunging wings at low reynolds numbers', *Journal of Fluids and Structures* **64**, 27–45.

Cook, P., Alavija, A. & Wildy, S. (2017), Identification and characterisation of delamination damage in composites utilising embedded optical strain gauges, *in* '9th Australasian Congress on Applied Mechanics', Engineers Australia, pp. 140–147.

Dieck, R. H. (2014), 'The purpose for measurements and understanding their uncertainties (the basic, iso and asme uncertainty models compared)'.

Ducoin, A., Astolfi, J. A. & Sigrist, J.-F. (2012), 'An experimental analysis of fluid structure interaction on a flexible hydrofoil in various flow regimes including cavitating flow', *European Journal of Mechanics-B/Fluids* **36**, 63–74.

Ducoin, A., Barber, R. B., Wildy, S. J., Codrington, J. D. & Baker, A. (2023), 'Experimental evaluation of the use of embedded fiber bragg gratings to measure steady and unsteady flow-induced marine propeller blade deformation', *Ocean Engineering* **281**, 114889.

Faure, T., Roncin, K., Viaud, B., Simonet, T. & Daridon, L. (2022), 'Flapping wing propulsion: Comparison between discrete vortex method and other models', *Physics of Fluids* **34**(3).

Gardner, A. D., Jones, A. R., Mulleners, K., Naughton, J. W. & Smith, M. J. (2023), 'Review of rotating wing dynamic stall: Experiments and flow control', *Progress in Aerospace Sciences* **137**, 100887.

Gordnier, R. E., Chimakurthi, S. K., Cesnik, C. E. & Attar, P. J. (2013), 'High-fidelity aeroelastic computations of a flapping wing with spanwise flexibility', *Journal of Fluids and Structures* **40**, 86–104.

Gupta, R. & Ansell, P. J. (2020), 'Flow evolution and un-

steady spectra of dynamic stall at transitional reynolds numbers', *AIAA journal* **58**(8), 3272–3285.

Heathcote, S., Wang, Z. & Gursul, I. (2008), 'Effect of spanwise flexibility on flapping wing propulsion', *Journal of Fluids and Structures* **24**(2), 183–199.

Herath, M. T., Phillips, A. W., St John, N., Brandner, P., Pearce, B. & Prusty, G. (2021), 'Hydrodynamic response of a passive shape-adaptive composite hydrofoil', *Marine Structures* **80**, 103084.

Hoffmann, M., Reuss Ramsay, R. & Gregorek, G. (1996), Effects of grit roughness and pitch oscillations on the naca 4415 airfoil, Technical report, National Renewable Energy Lab.(NREL), Golden, CO (United States); The Ohio ....

Holst, D., Church, B., Wegner, F., Pechlivanoglou, G., Nayeri, C. & Paschereit, C. (2019), 'Experimental analysis of a naca 0021 airfoil under dynamic angle of attack variation and low reynolds numbers', *Journal of Engineering for Gas Turbines and Power* **141**(3), 031020.

Janiszewska, J., Ramsay, R. R., Hoffman, M. & Gregorek, G. (1996), Effects of grit roughness and pitch oscillations on the ls (1)-0417mod airfoil, Technical report, National Renewable Energy Lab.(NREL), Golden, CO (United States).

Jumper, E., Schreck, S. & Dimmick, R. (1987), 'Lift-curve characteristics for an airfoil pitching at constant rate', *Journal of aircraft* **24**(10), 680–687.

Kerdraon, P., Horel, B., Bot, P., Letourneur, A. & David Le Touzé, D. (2021), 'High froude number experimental investigation of the 2 dof behavior of a multihull float in head waves', *Journal of Sailing Technology* **6**(01), 1–20.

McCroskey, W. J., McAlister, K., Carr, L., Pucci, S., Lambert, O. & Indergrand, R. (1981), 'Dynamic stall on advanced airfoil sections', *Journal of the American Helicopter Society* **26**(3), 40–50.

Mulleners, K. & Raffel, M. (2012), 'The onset of dynamic stall revisited', *Experiments in fluids* **52**, 779–793.

Paula, A. A. d. (2016), The airfoil thickness effects on wavy leading edge phenomena at low Reynolds number regime., PhD thesis, Universidade de São Paulo.

Pernod, L., Ducoin, A., Le Sourne, H., Astolfi, J.-A. & Casari, P. (2019), 'Experimental and numerical investigation of the fluid-structure interaction on a flexible composite hydrofoil under viscous flows', *Ocean Engineering* **194**, 106647.

Phillips, A. W., Cairns, R., Davis, C., Norman, P., Brandner, P. A., Pearce, B. W. & Young, Y. L. (2017), Effect of material design parameters on the forced vibration response of composite hydrofoils in air and in water, *in* 'Fifth International Symposium on Marine Propulsors', pp. 813–822.

Ramsay, R., Hoffman, M. & Gregorek, G. (1995), Effects of grit roughness and pitch oscillations on the s809 airfoil, Technical report, National Renewable Energy Lab.(NREL), Golden, CO (United States).

Reuss Ramsay, R., Hoffman, M. & Gregorek, G. (1996), Effects of grit roughness and pitch oscillations on the s815 airfoil, Technical report, National Renewable Energy Lab.(NREL), Golden, CO (United States); The Ohio ....

Robinson, M. & Wissler, J. (1988), Pitch rate and reynolds number effects on a pitching rectangular wing, *in* '6th Applied Aerodynamics Conference', p. 2577.

Seaver, M., Trickey, S. T. & Nichols, J. M. (2006), Strain measurements from fbgs embedded in rotating composite propeller blades, *in* 'Optical Fiber Sensors', Optica Publishing Group, p. ThD2.

Shayanpoor, A. A., Hajivand, A. & Moore, M. (2020), 'Hydroelastic analysis of composite marine propeller basis fluid-structure interaction (fsi)', *International Journal of Maritime Technology* **13**, 51–59.

Simonet, T., Roncin, K., Lapierre, L. & Daridon, L. (2020), Étude de l'efficience d'un système de propulsion maritime par foil oscillant souple, *in* '17èmes Journées de L'Hydrodynamique'.

Visbal, M. R. & Garmann, D. J. (2018), 'Analysis of dynamic stall on a pitching airfoil using high-fidelity large-eddy simulations', *AIAA Journal* **56**(1), 46–63.

Yeager, M., Whittaker, A., Todd, M., Kim, H., Key, C. & Gregory, W. (2017), 'Impact detection and characterization in composite laminates with embedded fiber bragg gratings', *Procedia Engineering* **188**, 156–162.

Young, Y. L., Garg, N., Brandner, P. A., Pearce, B. W., Butler, D., Clarke, D. & Phillips, A. W. (2018), 'Load-dependent bend-twist coupling effects on the steady-state hydroelastic response of composite hydrofoils', *Composite Structures* **189**, 398–418.

Young, Y. L., Valles, Z., Di Napoli, I., Montero, F. M., Minerva, L. F. & Harwood, C. (2023), 'Wave effects on the hydroelastic response of a surface-piercing hydrofoil. part 1. fully wetted and ventilated flows', *Journal of Fluid Mechanics* **963**, A37.

Zarruk, G. A., Brandner, P. A., Pearce, B. W. & Phillips, A. W. (2014), 'Experimental study of the steady fluid–structure interaction of flexible hydrofoils', *Journal of Fluids and Structures* **51**, 326–343.

Zhang, X. & Schlüter, J. U. (2012), 'Numerical study of the influence of the reynolds-number on the lift created by a leading edge vortex', *Physics of Fluids* **24**(6).